



## Micro-structural Deformation Field Analysis of Aluminum Foam using Finite Element Method and Digital Image Correlation

B. Akhavan<sup>a</sup>, A. Pourkamali Anaraki<sup>\*b</sup>, A. Malian<sup>c</sup>, Y. Taraz Jamshidi<sup>b</sup>

<sup>a</sup> Department of Industrial Engineering, IAU Tehran North Branch, Tehran, Iran

<sup>b</sup> Department of Mechanical Engineering, Shahid Rajaee Teacher Training University, Tehran, Iran

<sup>c</sup> Department of Civil Engineering, Surveying Group, Shahid Rajaee Teacher Training University, Tehran, Iran

### PAPER INFO

#### Paper history:

Received 23 February 2020

Received in revised form 19 June 2020

Accepted 26 August 2020

#### Keywords:

Digital Image Correlation

Response Surface Methodology

Aluminum Foam

Computed Tomography Imaging

Finite Element Method

### ABSTRACT

Porous materials especially closed-cell metallic foams play important roles among novel materials because of their good characteristics e.g. high strength to weight ratio and crashworthiness. On the other hand, mechanical behavior determination and detailed characterization are essential in efficient manipulation and material tailoring. In the present research especial hybrid experimental-numerical approach is used for aluminum foam behavior determination as to the main goal, i.e. continuous deformation field measurement using digital image correlation (DIC) and finite element analysis (FEA) on porous specimen's surface. To overcome the 3D modelling problem of closed-cell foams structure, we present the method based on CT-scan and digital optic microscope imaging combination. In the experimental part of the study, aluminum foams and proper specimens are manufactured, and then high-resolution digital imaging and illumination setup are employed. Finally, the deformation field is obtained using DIC. On the other hand, measurement verification and DIC parameters optimization processes are conducted using ABAQUS 2019 with comprehensive mesh independency study and response surface methodology (RSM) respectively as major research achievement. Finally, correlation equations based on high regression models are obtained. Using detailed geometrical micro-model and optimal DIC parameters yields to good numerical-experimental accordance. The novel approach of combined CT and digital microscope imaging instead of industrial micro-CT lowered imaging costs while yielded to accurate numerical results.

doi: 10.5829/ije.2020.33.10a.25

### NOMENCLATURE

$u, v$	Displacement concerning x and y axes	$H$	Shannon entropy (bit/pixels)
$\vec{P}$	Displacement vector	$DLP$	Dose length product (mGy.cm)
$LS$	Least squares correlation	$CTDI$	CT-scan dose index (mGy)
$f, g$	Gray level function in reference and current configurations	$L_s$	Scan length (cm)
$n$	Subset size (pixels)	$HU$	Hounsfield unit
$H(\vec{P})$	Hessian operator	$SNR$	Signal to noise ratio
$E$	Small strain tensor	$S_{subset}$	Subset size (pixels)
$\varepsilon$	Strain tensor	$R_{subset}$	Subset radius (pixels)
$ZNCC$	The zero-mean normalized sum of squared differences	$SFOV$	Scan field of view

## 1. INTRODUCTION

Novel methods of experimental stress and strain analysis play an important role in material behavior

characterization. For instance, using rosettes were the most reliable approach in mechanical parameters extraction. Although they had several problems such as adhesive effect, discrete strain field determination, high

\*Corresponding Author Institutional Email: [ali\\_pourkamali@sru.ac.ir](mailto:ali_pourkamali@sru.ac.ir)  
(A. Pourkamali Anaraki)

operational cost, impossible to use on porous surfaces, etc. Digital image correlation (DIC) is one of the most efficient approaches that overcome many of the mentioned disadvantages. Digital image correlation is a technique that attempts to find correlations and similarities between the reference image segment and deformed configuration. Skozrit et al. [1] investigated elastic-plastic and failure of various aluminum alloys both numerically and experimentally. They conducted static and dynamic tensile tests and also three-point bending experiment with different strain rates. They manipulated the two-dimensional plane stress finite element analysis. For validation purposes in the displacement and strain field, they performed several DIC measurements. Also, they used infrared thermography as an efficient tool for damage propagation survey. The digital correlation technique also used for material parameter identification as well [1]. Begonia et al. [2] studied strain and displacement field in mouse forearm bone using a non-contact DIC method under uniaxial compression loading. The digital image correlation method is employed on mechanical characterization and deformation measurement of two dimensional SiC/SiC composite pipes [3]. Mehdikhani et al. [4] studied the deformation field and whole strain tensor of the composite cross-section and its fibers in the micro-scale. Their investigations are focused on using the DIC technique with the SEM images for three-point bending tests of fiber-reinforced laminates.

Due to the brilliant high-temperature behavior of ceramic matrix composites, Whitlow et al. [5] conducted comprehensive in-situ health monitoring of SiC/SiC and their service life using the DIC method. They studied the ultimate strength and effects of fiber properties on it. Gerbig et al. [6] coupled the conventional finite element method with the DIC technique. The estimated material parameters corresponded to the non-uniform displacement distribution in the tensile test specimen. They also used an optimization approach for validation purposes. Engqvist et al. [7] studied strain field and deformation mode of loaded glass polycarbonate using DIC. They loaded novel specimen bi-axially for localized strain investigations. Opera et al. [8] used infra-red thermography and image processing in metal dynamic yield behavior determination. For comparison purposes, they used 3D digital image correlation. Ceramic blocks and composite resins are widely used in dentistry. Jiang et al. [9] studied the stress intensity factor in these materials using the DIC method. In such small parts, it is impossible to use conventional stress analysis and standard specimens. Nguyen et al. [10] investigated the mechanical behavior of cortical bone using a multi-scale micro-macro method and DIC technique. They captured images in both scales during the loading condition. The main goal is to determine material properties on several scales. A wide range of composite applications and

complex nature of fatigue and crack growth using classical methods are the main research idea. Aparna et al. [11] studied cracking and stress intensity measurement using DIC in the fatigue test of GFRP. Feng et al. [12] studied the effects of fiber reinforced polymer confinement technique to overcome the drawbacks of rubberized concrete. Statistical models were also developed based on experimental using response surface methodology (RSM). Finally, the regression analysis was performed to develop response equations based on quadratic models. Obianyo et al. [13] investigated the efficiencies of sedimentation tanks with horizontal and vertical baffle mixers, and also determined the optimal values of factors of clarification in the sedimentation tanks. Response surface methodology was further used for the present analysis of data in this study for more reliable study because it optimized the responses of variables. Sharif et al. [14] studied the use of cellulose dust produced in the drying section of paper mills as a potential adsorbent to remove methylene blue dye. They manipulated the RSM or simply the response surface methodology with CCD which stands for central composite design. Yang et al. [15] investigated the effect of using aluminum foam in sound absorption application for mining industry. They showed that using this kind of porous material yielded to the noise reduction in mining chute. In addition to, the aluminum foam has major positive effect on vibration reduction. Hosseini Ravandi et al. [16] manipulated the image processing technique for lightness change of fabric appearance. He also used ANOVA technique for correlation measurement purposes. Fattahzade et al. [17] presented the new approach of monitoring using sequential images. They used statistical methods and measured correlation between images for defect detection process.

In the present paper, digital images captured during the uniaxial compression test of aluminum foams are analyzed using the DIC technique. So continuous displacement and strain fields are measured on the external surface of the specimen. These results could be used in the stress field, energy absorption capacity, and also material parameters identification. The procedure is categorized into several steps such as specimen manufacturing and preparation for a compression test, imaging system and illumination setup, DIC-based measurement using initial setting, DIC parameters optimization using RSM, and validation process using FE simulations. Also, an analysis of variance is used for response regression and significant factors determinations. For high accuracy FE analysis, micro-structural foam modeling is performed using CT-scan and digital optic microscope. Because micro CT is an expensive procedure, we used a conventional CT-scan device. To enhance the modeling resolution, mesh refinement technique is employed using the optical microscope imaging. Using CT-scan instead of micro-CT

for geometric modeling with acceptable accuracy is considered as a novelty. Furthermore, using RSM-based optimization enhances the deformation field estimation with high desirability value. Finally, FE results and DIC measurement calculations are in good agreement. The whole research process and methodology is illustrated in the following flowchart (see Figure 1). After the introduction section which consists of literature review and process flowchart, the materials and methods section is appeared. This section consists of sample preparation process and uniaxial test method, DIC method theoretical aspects and modeling techniques using CT-scan. The next section consists of results interpretation and discussion, verification methodology, and parametric study and optimization using DOE and RSM techniques. The last section consists of conclusions and major research findings.

## 2. MATERIALS AND METHODS

### 2. 1. Specimen Preparation and Uniaxial Compression Test

Aluminum foams are employed as the main material used in the present research. The mentioned Alporas foams are manufactured using liquid state method with 2% TiH<sub>2</sub> and 1.5% Calcium. Additives are used as the blowing agent and viscosity enhancer respectively, at 680 deg. Manufactured blocks have 100×50×10 cm dimensions. Precision sizing of specimens is performed by CNC milling. Finally, several aluminum foam specimens are prepared and sized for

compression tests. Present foam specimen densities are generally 300 and 500 kg/m<sup>3</sup> depending on the location in the manufactured block. Because of the melt hydrostatic pressure and bubble growth, the bottom half of the block has 500 and the top half has 300 kg/m<sup>3</sup> densities respectively. Standard uniaxial tension test is conducted to determine the mechanical properties of aluminum foam, according to ASTM B557. Mechanical behavior analysis of cubic closed-cell aluminum foam specimens is performed using quasi-static compression testing using ZWICK 100 apparatus with a five mm/min loading rate. Prepared specimens and loading device are shown in Figure . Prepared specimens have approximately 40×40×40 mm dimensions to ensure at least six complete cells in each direction. This guarantees rather a uniform deformation without localized failure and collapses. Furthermore, specimens are prepared large enough for better imaging and illumination during compressive loading. Specimen density in the present research is 500 kg/m<sup>3</sup>.

### 2. 2. Digital Image Correlation Technique Implementation

Digital image correlation is a technique of finding correlation and similarities between the reference image and deformed configuration in loading conditions. So, images are discretized initially to several subsets. Comparing reference and possible current subsets lead to displacement vector calculation. Using small deformation assumption in any increments, we have equations for displacement vector components in every pixel as below (Equations (1)-(3)) [18].

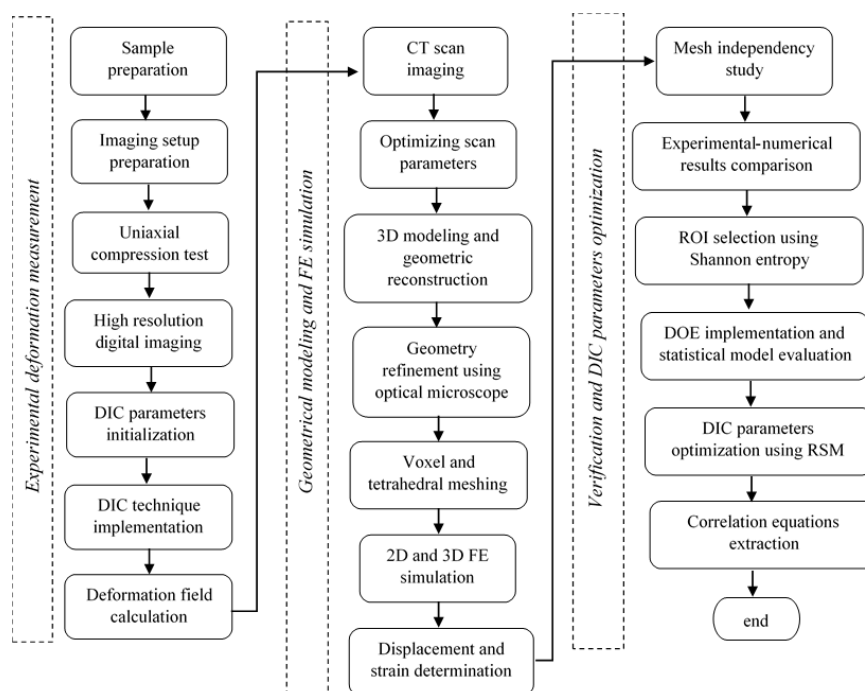
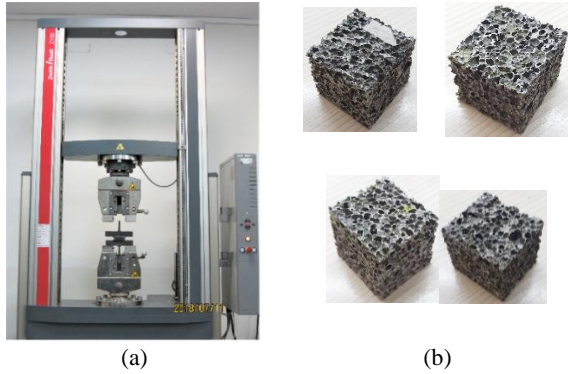


Figure 1. Research process and methodology flowchart



**Figure 2.** Zwick100 loading device (a), and prepared specimens for uniaxial compression test (b)

$$u_s = u + \frac{\partial u}{\partial x} \Delta x + \frac{\partial u}{\partial y} \Delta y \quad (1)$$

$$v_s = v + \frac{\partial v}{\partial x} \Delta x + \frac{\partial v}{\partial y} \Delta y \quad (2)$$

Furthermore, the main DIC objective is focused on displacement vector determination  $\vec{P}$  (Equation (3)).

$$\vec{P} = \left\{ u, \frac{\partial u}{\partial x}, \frac{\partial u}{\partial y}, v, \frac{\partial v}{\partial x}, \frac{\partial v}{\partial y} \right\}^T = \{P_i\}^T, i = 0, \dots, 5 \quad (3)$$

There are several correlation definitions such as cross-correlation, CC and least squares, LS (Equation (4)). In the present paper, the least square method is used to obtain accurate results. Furthermore, we manipulate ZNCC correlation formulation to lower the noise sensitivity problem. Hence:

$$LS = \frac{\sum_{i,j=-\frac{(n-1)}{2}}^{+\frac{(n-1)}{2}} \{f(x,y) - g(x^*,y^*)\}^2}{\sum_{i,j=-\frac{(n-1)}{2}}^{+\frac{(n-1)}{2}} f(x,y)^2} \quad (4)$$

In which  $n$  is subset size, and  $i$  and  $j$  are pixel counters. Functions  $f$  and  $g$  are gray levels in reference and current configuration. Deformed subset finding is equivalent to the minimum  $LS$  value. Newton-Raphson approach is employed for the minimization procedure, as formulated in Equation (5). So

$$\nabla LS = \frac{\partial LS}{\partial P_k} = \frac{2}{\sum_{i,j=-\frac{(n-1)}{2}}^{+\frac{(n-1)}{2}} f(x,y)^2} \cdot \sum_{i,j=-\frac{(n-1)}{2}}^{+\frac{(n-1)}{2}} \{f(x,y) - g(x^*,y^*)\} \frac{\partial g}{\partial P_k} \quad (5)$$

Using the  $\vec{P}_0$  as an initial displacement vector components estimates, the general Newton-Raphson form appears as below (Equation (6)).

$$\vec{P}_{n+1} - \vec{P}_n = -H(\vec{P}_n)^{-1} \cdot \nabla LS(\vec{P}_n) \quad (6)$$

In which  $H$  is the Hessian operator. Using the iterative procedure, the displacement vector  $\vec{P}$  is calculated within the desired tolerance [19]. Also, using high-resolution

images and proper filtering may help increase measurement accuracy [20]. After displacement field calculation, strain tensor components could be determined using kinematic equations as below. Using small displacement assumption, these equations reduced to (Equations (7)-(9))

$$E_{xx} = \frac{\partial u}{\partial x} \quad (7)$$

$$E_{yy} = \frac{\partial v}{\partial y} \quad (8)$$

$$E_{xy} = \frac{1}{2} \left( \frac{\partial u}{\partial y} + \frac{\partial v}{\partial x} \right) \quad (9)$$

**2. 3. Noise and Illumination Sensitivity** During the experiments and imaging process, noise and light illumination variations are inevitable. Hence, using correlation criteria with minimum sensitivity to these alternations in the DIC method is essential. Main noise sources are summarized as light variation during specimen deformation, low image resolution, inaccurate focus, or even lens distortion effects. There are many criteria such as cross-correlation, normalized cross-correlation, the sum of squared differences, and the zero-mean normalized sum of squared differences, ZNCC (Equations (10), (11)). The latter criterion is one of the most efficient definitions in noisy conditions. In the present paper, ZNCC and LS are used as correlation criteria [21]. So,

$$C_{ZNCC} = \sum_{i=-M}^M \sum_{j=-M}^M \left\{ \frac{[f(x_i,y_j) - f_m] \times [g(x_i^*,y_j^*) - g_m]}{\Delta f \Delta g} \right\} \quad (10)$$

In which  $M = (n - 1) / 2$ . Also, we have

$$f_m = \frac{1}{(2M+1)^2} \sum_{i=-M}^M \sum_{j=-M}^M f(x_i, y_j) \quad (11)$$

$$\Delta f = \sqrt{\sum_{i=-M}^M \sum_{j=-M}^M [f(x_i, y_j) - f_m]^2}$$

$$g_m = \frac{1}{(2M+1)^2} \sum_{i=-M}^M \sum_{j=-M}^M g(x_i^*, y_j^*)$$

$$\Delta g = \sqrt{\sum_{i=-M}^M \sum_{j=-M}^M [g(x_i^*, y_j^*) - g_m]^2}$$

Subset size plays an important role in DIC calculations. Subset size selection is a trade-off between several factors such as deformed subset discovery probability and results accuracy. In other words, using too small subset leads to improper subset finding. On the other hand, a large subset size increases the computational error. During deformation, it is possible to occur subset infinitesimal deformation in the sub-pixel scale. Due to the discrete nature of image gray values, sub-pixel calculations are meaningless [21]. To overcome the mentioned limitation, the bi-cubic interpolation technique is employed as shown in Figure . In this figure, horizontal  $x$  and  $y$  plane are pixel coordinates and the

vertical axis is gray values related to each pixel. Proper bi-cubic interpolation shows good agreement with actual gray values.

**2. 4. Speckle Pattern Evaluation and Entropy Determination** One of the most important factors affecting displacement field calculations is speckle pattern or simply gray index distribution and randomness. Shannon entropy is used to evaluate the quality of random patterns. This criterion is actually information contents expected value in a gray-scale image (Equation (12)). So,

$$H = \sum_{k=0}^M p_k \log\left(\frac{1}{p_k}\right) \quad (12)$$

In which  $H$  is Shannon entropy in bit per pixels,  $p_k$  is the normalized probability of each gray values, and  $M = 255$  is the number of gray value in each pixel, i.e.  $2^\beta - 1$  for  $\beta$ -bit images. Parameter  $p_k$  could be obtained using the image histogram. To enhance the DIC calculation accuracy and proper region-of-interest (ROI) selection, entropy values are determined for different sections of reference images. Maximum entropy leads to more accurate results. In Figures 4 and 5 four different regions with high entropy values and their corresponding histogram are shown. These regions are chosen to be manipulated as optimum ROIs. As shown, entropy values are within 7.28 to 7.53. Despite the fact, there are approximately random speckle patterns on specimens due to the manufacturing process, cutting, machining, and grinding, we used several other methods such as paint spraying and abrasive papers in order to enhance entropy values [22].

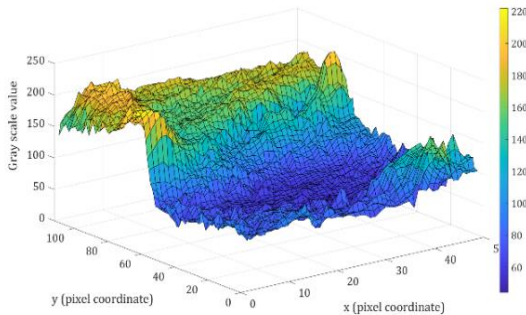


**Figure 3.** Bi-cubic interpolation of gray levels used in sub-pixel displacement determination

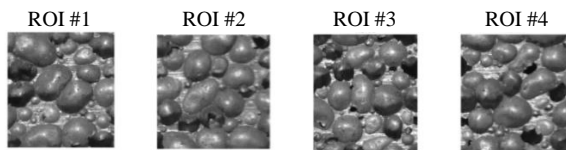


**Figure 4.** Four reference image segments with high entropy

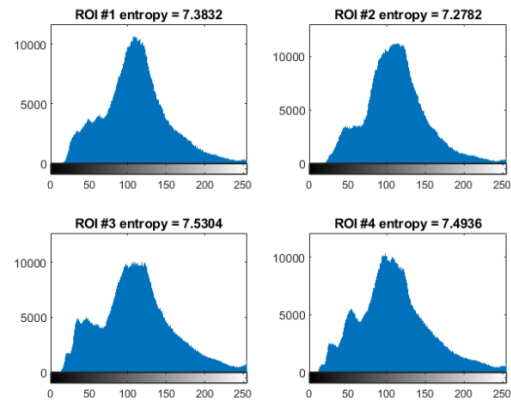


**Figure 5.** Four reference image segments histograms and Shannon entropy

**2. 5. Micro-Structure Modeling Using Digital Images and Computed Tomography**

Using computed tomography is a newly emerged technique in geometric modeling of cellular microstructure. So we use the CT-scan device on prepared specimens for modeling purposes. As mentioned, using low-cost CT instead of micro-CT for 3D modeling is considered as an advantage. Furthermore, we choose for several CT imaging settings and protocols to enhance the modeling quality. Finally, the optimum values for CT imaging parameters are obtained. In the present research, the CT-scan device is *GE 16 slices* with 0.1 to 0.2 mm slice thickness, small scan field of view (SFOV) of 154, 120 kV voltage, 100 mA current, and 1-s full helical scan setting. The mentioned settings are chosen after the iterative process of optimization and qualitative evaluation of captured images. Significant parameters are voltage, current, slice increment, and scan field of view. Voltage variation levels are 100, 120, and 140 kV. It is seen that decreasing current leads to an increase in image noise and artifact. Although the image contrast may increase slightly. On the other hand, the increasing voltage to 140 kV does not control image noise considerably. So the optimum voltage is chosen to be 120 kV. For the present CT-scan device, there are three current options in the aforementioned voltage. The proper values are 80, 100, and 120 mA [23]. Corresponding to the present scan condition, volumetric CT-scan dose index,  $CTDI_{vol}$  is 37.17 mGy, dose length product, DLP (formulated in Equation (13)) is 297.6 mGy.cm, dose efficiency is 85.7%, radiation exposure time is 14.2 s, and the phantom length is 16 cm [24]. So we have:

$$DLP(mGy \cdot cm) = CTDI_{vol}(mGy) \cdot L_s(cm) \quad (13)$$

In which  $L_s$  is scan length. The specimen's scan dimension is about 8 cm. After scanning with optimum settings, the diVision Lite commercial software is used for quality evaluation. In Figure 6 one CT-scan slice of

two different foam specimens is shown. Artifact occurrence is severe in metal CT images especially metallic foams. Using optimum settings and proper protocol minimizes the undesired effects [25]. Image enhancement and noise reduction are achieved using a non-linear median filter [20]. Foam specimens used in CT-scan imaging have the approximate dimension of 58×40×41 and 46×43×42 mm. We crop desired specimens corresponding to the uniaxial compression experiments for simulation purposes after 3D modeling. The 3D models used in FE simulations are cubes with at least approximately 40 mm dimension. Another significant parameter affecting 3D geometric reconstruction is the CT-scan threshold measured with the Hounsfield unit (HU). This index corresponds to the distinction capability of metal from voids [26]. Altering the HU lead to different model densities. Knowing the 300 to 500 kg/m<sup>3</sup> density range of aluminum foam is equivalent to -500 to 500 HU [27].

The current increase is similar to the voltage parameter. So the optimum current value is chosen to be 100 mA. Goal functions in CT-scan parameters are signal to noise ratio, SNR and contrast to noise ratio SNR. The scan field of view is chosen corresponding to the specimen dimensions. In contrast to mA and kV, an increase in SFOV leads to noise increases. The Mimics Research 21.0 commercial software is used for modeling purposes [28]. In Figure 7 the whole process of 3D geometric reconstruction is shown.

**2. 6. Mesh Generation Using Voxel and Tetrahedral Elements**

Mesh generation is the most important step in FE simulations. In the present research, we used two types of elements for comparison

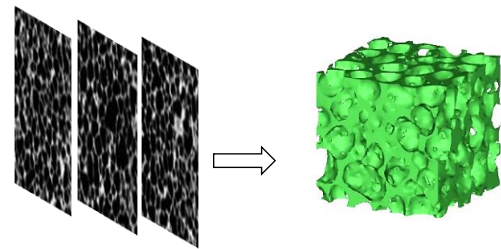


**Figure 7.** Process of 3D model reconstruction in Mimics using CT-scan slices

purposes, i.e. 8-noded voxel brick and 4-noded tetrahedral element with linear interpolation shape function. Each approach has its unique merits and disadvantages. Voxel elements have a minimum computational cost because they have the minimum number of nodes and elements. Because they have jagged geometry, they did not fit geometry completely. Using tetrahedral elements may help overcome this problem especially in the curved regions. Although using a 4-noded element leads to the dramatic increase in computational cost. Another disadvantage is related to the higher error in deformation field calculations. Refining tetrahedral mesh could help to enhance the calculations [29]. In Figure two types of finite element models with tetrahedral and brick elements are shown.

To obtain the optimum mesh density with acceptable accuracy and relatively low computational cost, four FE models are generated and simulations are performed. In Table 1 mesh independency analysis results are shown. In this table, computation cost and results agreement index are given in normalized form concerning optimum

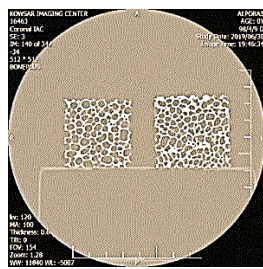


**Figure 6.** CT-scan slice image quality evaluation for two different metallic foams in diVision Lite

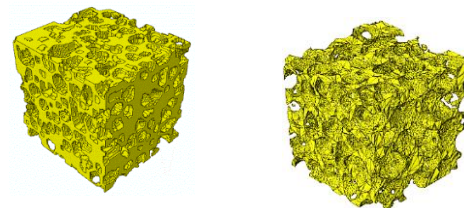


**Figure 8.** Finite element model of cellular solid using CT-scan images, (a) Voxel brick element and (b) tetrahedral element

**TABLE 1.** Mesh independency study for different mesh size

Agreement with Ref. solution	Normalized computation time	App. Node no. (×1000)	App. Element no. (×1000)	Voxel size	Mesh density	Mesh geometry
1.02	5.3	1817	1169	1	fine	
1.0	1.0	348	206	2	Relatively fine	Hexahedral brick (Voxel)
1.56	0.45	122	72	3	Average	
0.25	0.12	42	25	4	Coarse	

mesh density, i.e. relatively fine. As observed, using fine mesh leads only 2% results variations but 5 times increase in computational cost. On the other hand, using average and coarse mesh increase calculation error to 56 and 75%.

### 2. 7. Finite Element Simulation Implementation

Finite element simulation with explicit dynamic step and reduced loading rate is performed for quasi-static results using ABAQUS commercial software. Optimized mesh contained hexahedral brick C3D8 and tetrahedral C3D4 elements. The universal loading device plateau is modeled using R3D4 rigid elements. To obtain smooth results with minimum noise, anti-aliasing and Butterworth filters with 2kHz cutoff frequency are employed [30]. Simulation inputs and material properties are obtained using tensile tests with ASTM B577 standard [31] as shown in Table 2.

## 3. RESULTS AND DISCUSSIONS

### 3. 1. Displacement And Strain Field Measurement Using DIC

In this section, digital images captured during the compression test of aluminum foam specimens are used to obtain displacement and strain field using the DIC technique. Digital image correlation

outputs are displacement vector ( $u, v$ ) and strain tensor ( $\epsilon_{xx}, \epsilon_{yy}, \epsilon_{xy}$ ). The process of field variable determination has many parameters affecting output accuracy. These parameters are summarized as current and reference configuration, ROI, subset size, subset spacing, solution tolerance, calibration factor, lens distortion factor, strain radius, etc. Generally, predefined settings are proper and DIC outputs have a relatively low computational error. But DIC implementation for the porous surface of foams requires iteration for proper settings selection to avoid solution divergence. In Table 3 initial settings are illustrated. In the later section, we employ RSM based optimization to find optimum parameters of DIC to achieve minimum error. Altering various settings lead to significant parameter identification. In brief, the most significant factors in displacement field calculation are subset radius and subset spacing both in pixels. For strain measurement, there is one more factor, i.e. strain radius. For validation purposes, displacement vector and the strain tensor components are compared with corresponding FEA results in a particular point as shown in Figure 9.

After DIC implementation, horizontal displacement  $u$ , and vertical displacement  $v$  are obtained in continuous contour form. It is worth noting that  $v$  displacement contour is smoother than  $u$  contour. It is because of the mechanical behavior of porous solids. In other words,

TABLE 2. Material mechanical and physical properties used in FE simulation

Poisson's ratio	Yield strength (MPa)	Tangent modulus (GPa)	Young's modulus (GPa)	Mass density (kg/m <sup>3</sup> )	Material
0.35	76	0.47	69	2700	Aluminum

TABLE 1. Initial DIC parameters

Max. allowable iterations	Solution tolerance	Strain radius (pixel)	Subset spacing (pixel)	Subset radius (pixel)	ROI size (mm)
60	1.0e-7	15	1.0	34	20-40
Solution	Loading disp.	Frame No.	Seed position	Thread No.	ROI shape
direct	0.576 mm	20	Quarter ROI	4-8	Rectangular

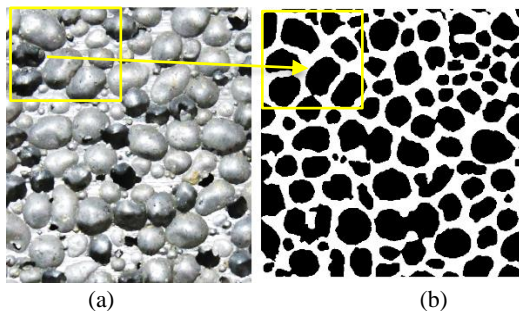


Figure 9. The particular point used for validation purpose and field measurement, (a) digital image and (b) filtered binary image for FE modeling

the displacement field in direction of loading is quite smooth but because of the low Poisson's ratio and localized cell buckling, there is a non-smooth contour and a high amount of computational error in the transverse direction. Vertical and horizontal displacements are measured using DIC after averaging field values in the neighboring region. These values are 0.35 and 0.07 mm. To ensure the validity of the results, three distinct compression experiments are performed and their results are reported as an average value. In addition, the DIC procedure is done for strain measurement calculation. The strain field calculation is  $\epsilon_{xx}$ ,  $\epsilon_{yy}$  and  $\epsilon_{xy}$  measurement. Due to the small values,

normal strains are reported as percent and shear strain is reported as a degree. A higher computational error in strains is due to the derivation of the displacement field. Although there is a smooth contour in the strain field, because of the averaging and interpolation process. The contour smoothness in strain calculation is related to the strain radius parameter. Normal vertical and horizontal strains are -0.7 and 1.2% and shear strain is 1.6°. Strain field is a combination of both tensile and compressive normal strain because of the localized nature cell walls and faces deformation.

**3. 2. Results Verification Using FEA and DIC**

Because of the porous nature of the metallic foam, it is impossible to use contact methods of strain measurement such as strain rosettes. Furthermore, many experimental methods cannot determine the field variable in continuous form. So for verification purposes, FE analysis is chosen. In this way, the major requirement is accurate geometric modeling and meshing for simulation. As mentioned before, CT-scan images and digital microscopy techniques are employed in geometric reconstruction and modeling. Digital microscopy images with 800X zoom are used in micro-structural details refinement e.g. cell edge, that rather low-resolution CT-scan failed to model. In Figure 10 it is shown that cell edge thickness varies from 0.2 to 0.4 mm. using this method, the FE model updated with actual values of micro-structural feature dimensions and hence true foam relative densities are obtained in modeling.

FE simulation results compared to DIC outputs of aluminum foam are shown in Figure 11. In these contours, v-displacement and u-displacement are shown.

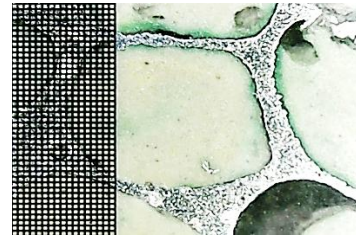


**Figure 10.** Digital microscope image used in micro-structural detail measurements with a scale of 0.1 mm

These values are approximately 0.4 and 0.083 mm. Hence, relative errors corresponded to the DIC measurements are 15 and 19% respectively. The error values show good agreement between DIC and FEA outputs. Furthermore, strain tensor components are obtained within the FE analysis. So  $\epsilon_{yy}$ ,  $\epsilon_{xx}$ , and  $\epsilon_{xy}$  are -1.08, 0.161, and 2.6°. DIC relative errors in strain field measurements are 55, 34, and 65%. A higher amount of error is related to the derivation operator in strain calculation from the displacement field.

As it is mentioned, strain components contour plots are FEA and DIC main results. So in Figure 12 the normal and shear strain contours are shown. Furthermore, the FEA outputs are compared to the DIC results. As it is obvious, there are more discontinuity rather than displacement contours. It is because of the inherent error of derivation operator. It is worth noting that normal and shear components of strain tensor are measured higher than FEA values. It guarantees that we can rely on the DIC values and in this way we are on the safe side.

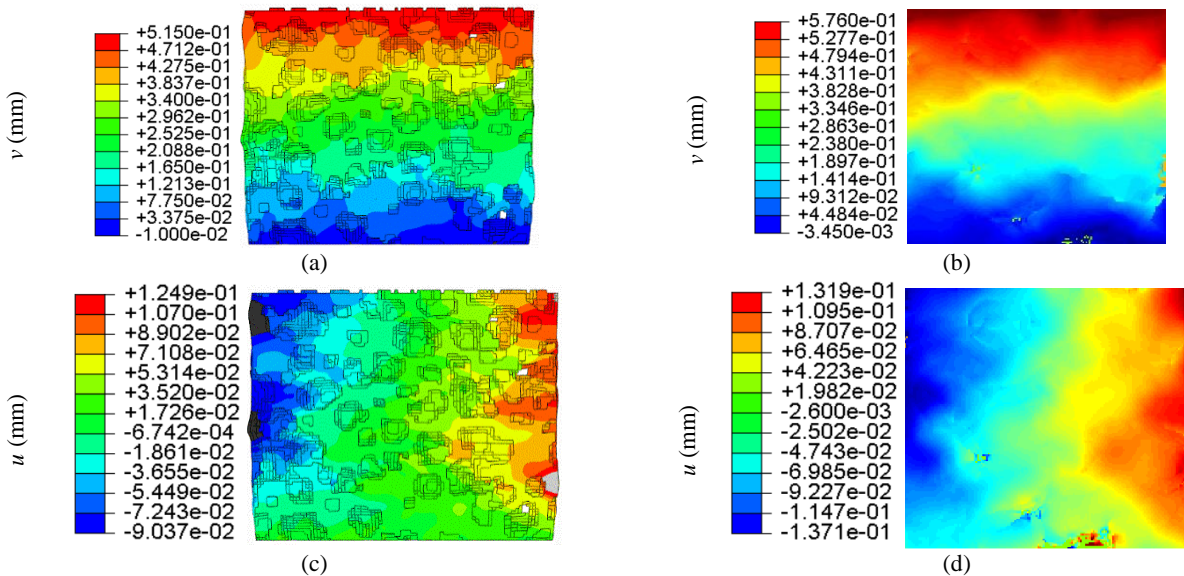


**Figure 11.** Displacement field determined by FEA on the porous surface of foam specimen, (a) FEM v-disp., (b) DIC v-disp., (c) FEM u-disp., and (d) DIC u-disp

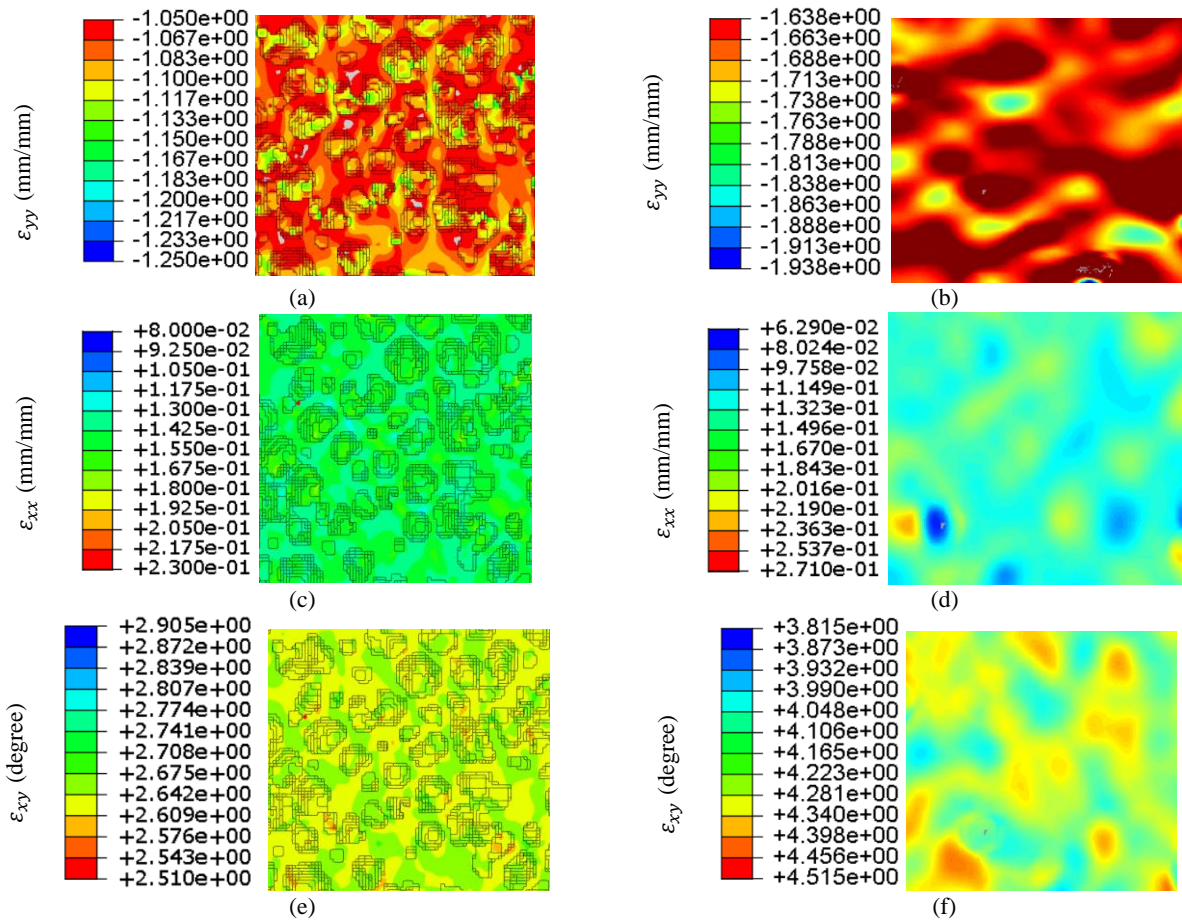


**Figure 12.** Strain field determined by FEA on the porous surface of foam specimen, (a) FEM  $\epsilon_{yy}$ , (b) DIC  $\epsilon_{yy}$ , (c) FEM  $\epsilon_{xx}$ , (d) DIC  $\epsilon_{xx}$ , (e) FEM  $\epsilon_{xy}$ , (f) DIC  $\epsilon_{xy}$

Mehdikhani et al. [4] are also compare the FEA and DIC results. But they used 2D cross-sectional model of micro fibers. We modeled the porous media with detailed micro-structure in 3D space. Also they used free meshing technique with the triangular element in contrast to the structured voxel mesh in the present research. As a comparison to the previous research, it is worth noting that Begonia et al. [2] studied porous media also. They investigated the mechanical behavior of mouse forearm in micro-scale. Also, they studied the method of finding proper ROI for DIC implementation. They used the iterative approach, while we manipulated the Shannon entropy methodology.

**3. 3. Experimental Design and DIC Output Effective Factors Identification** In the previous section, displacement and strain field variables are illustrated in the form of contour plots. Variables are determined using initial settings. The main goals of the design of experiments (DOE) and response surface methodology (RSM) implementation are the identification of important factors in DIC response and

also optimizing these factors to obtain measurements with minimum error. Using five levels RSM with the central composite design approach instead of the conventional factorial method helps to decrease the number of experiments and also increases the accuracy. There are two factors and two responses in DIC measurement of displacement, i.e. subset radius and spacing as factors and u-disp. and v-disp. as responses. For strain measurement, there are three factors and responses namely, subset radius, subset spacing, and strain radius as factors and  $\epsilon_{yy}$ ,  $\epsilon_{xx}$ , and  $\epsilon_{xy}$  as responses. These parameters and their corresponding levels are summarized in Table 4.

Finally, several DOE runs are performed with displacement and strain measurements for various factor levels. These factors and corresponding responses for displacement prediction using DIC are summarized in Table 5. Note that the average DIC value of the leverage parameter for the whole experimental design is 0.4615. It guarantees that no need to repeat any experiment. Due to the  $R^2$  and adjusted  $R^2$  with 0.906 and 0.8388 values for u-disp. and 0.7911 and 0.6418 for v-disp., the quadratic

**TABLE 2.** Factors and levels used in DOE with RSM

Analysis	$-\alpha, +\alpha$ (-2,+2)	Low (-1)	Mean (0)	High (+1)	Brief symbol	Symbol	factor
Disp. and strain	26, 42	30	34	38	A	$R_{subset}$	Subset radius
Disp. and strain	0, 4	1	2	3	B	$S_{subset}$	Subset spacing
strain	5, 25	10	15	20	C	$R_{strain}$	Strain radius

**TABLE 3.** Experimental design and displacement vector responses from DIC

Std. order	Run No.	$R_{subset}$ (pixel)	$S_{subset}$ (pixel)	$u$ (mm)	$v$ (mm)
4	1	38	3	0.0768	0.3595
3	2	30	3	0.0663	0.3465
12	3	34	2	0.0718	0.3545
11	4	34	2	0.0725	0.3495
6	5	42	2	0.0886	0.392
2	6	38	1	0.0793	0.371
13	7	34	2	0.0742	0.356
10	8	34	2	0.0686	0.3465
9	9	34	2	0.0707	0.364
5	10	26	2	0.0847	0.3745
7	11	34	0	0.0863	0.399
1	12	30	1	0.0895	0.4025
8	13	34	4	0.0779	0.392

model is selected. Considering Box-Cox graphs for u-disp. and v-disp. shows that the optimum  $\lambda$  values are 1.7 and -2.5.

Analysis of variance is used for displacement and strain regression. Results show that in v-disp. regression subset radius squared and subset spacing squared terms are significant because they have the lowest p-values. In other words, p-values less than 0.05 and more than 0.1 have corresponded to the significant and insignificant terms respectively. Furthermore, the degree of freedom related to both responses is five. So u-disp. and v-disp. regression equations (Equations (14), (15)) are as below. Note that the brief symbol of each factor is used.

$$(u)^{1.5} = 0.0192 + 0.0003A - 0.0015B + 0.0022AB + 0.0016A^2 + 0.0011B^2 \quad (14)$$

$$(v)^{-2.5} = 13.47 - 0.1300A + 0.5247B - 0.8608AB - 0.5962A^2 - 0.8096B^2 \quad (15)$$

To guarantee model validity, there are several criteria. Four major criteria are the Box-Cox graph, the normal plot of residuals, plot of predicted values vs. actual, and also residuals vs. predicted values. In Figure 13 four

important plots are shown for u-disp. response. Firstly the Box-Cox offers  $\lambda = 1.7$ . Non-curved plot of residuals also is required as an index of validation. Also predicted vs. actual values show good agreement. Finally, the random distribution of externally studentized residuals with -3 to +3 values is good enough. In Figure 14 contour plot and the spatial surface of u-disp. the response is shown.

Considering the results shows that there is a negligible perturbation in mid-point neighbor. Although, the effect of subset spacing is generally descending and the effect of subset radius is descending and ascending for values less than mid-point and more than mid-point respectively. In a small subset radius, the negative slope of subset spacing has significant growth. On the other hand, in large subset spacing, the ascending effect of the subset radius is significant. Analyzing strain responses also lead to quadratic model regression. In strain regression, minimum  $R^2$  and adjusted  $R^2$  values are 0.82 and 0.65. Strain equations with quadratic form have nine degrees of freedom. Also, the four aforementioned criteria are controlled to ensure the model validity. Perturbation plots of strain regressions show that horizontal strain sensitivity in mid-point has concave upward variation behavior. In vertical strain, there is similar behavior for subset radius with horizontal strain. In shear strain, subset radius and strain radius have ascending and descending variations respectively. Subset spacing also has downward convex variation. Strain radius has the most significant effect in vertical and shear strains. Considering the analysis of variance results shows that the most important term in vertical and horizontal strains is subset radius squared. In shear strain regression, the most important terms are strain radius and subset spacing squared.

### 3. 4. Effective Factors Optimization of Field Variables Determination

After modeling desired responses using quadratic regression, the optimization process is performed to find optimum DIC setting parameters to obtain results with minimum error. Based on validated and verified FE outputs, these values are considered as the goal values. Goal responses are 0.083 and 0.4 mm for u-disp. and v-disp. Furthermore, the optimization constraints are the actual factor ranges in DOE. In Table 6 optimization results for displacement measurement using DIC are summarized. According to

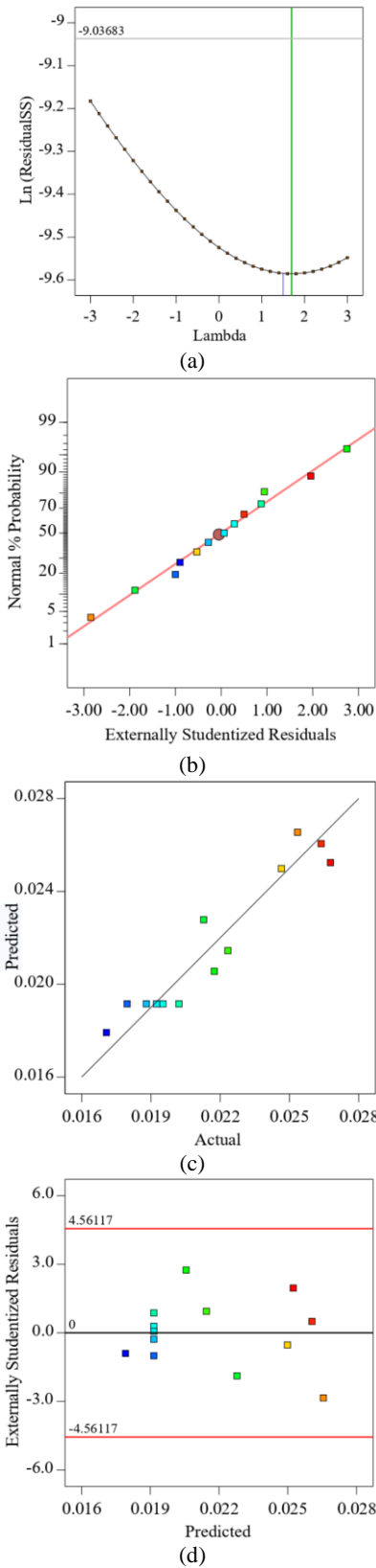


**Figure 13.** Statistical criteria for model evaluation, (a) Box-Cox plot, (b) normal residuals, (c) actual vs. predicted values, and (d) residuals vs. predicted values

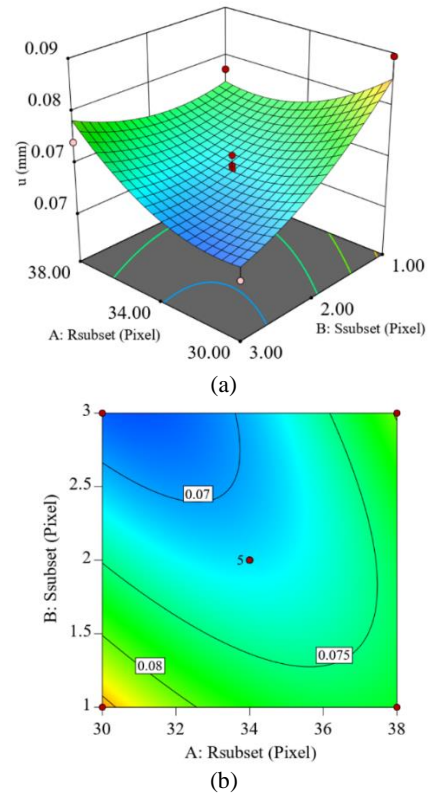


**Figure 14.** Regression of u-disp. response, (a) spatial surface representation, and (b) contour plot

the optimization results, there are eight solutions with desirability from 71 to 41%. Selecting a proper solution has corresponded to two aspects, i.e. higher desirability and integer number in factors. Another point is that we should analyze desirability values according to each response separately in addition to combined desirability. Considering the whole solutions lead to  $R_{subset} = 30$  and  $S_{subset} = 1$  for displacement measurement using DIC. It is worth noting that the mentioned solution is not unique for strain components too. So the optimization process is performed for strain measurement.

Strain factor optimization leads to 53 solutions with 82 to 31% desirability. The first solution has 82%

**TABLE 4.** Optimization results for displacement measurement using DIC

desirability	v	u	$S_{subset}$	$R_{subset}$	No.
0.712	0.387	0.086	1.000	30.000	1
0.707	0.386	0.086	1.024	30.000	2
0.689	0.383	0.085	1.091	30.000	3
0.591	0.376	0.080	3.000	38.000	4
0.574	0.375	0.080	2.963	38.000	5
0.572	0.375	0.080	3.000	37.864	6
0.427	0.368	0.077	1.000	38.000	7
0.413	0.367	0.077	1.000	37.400	8

combined desirability. Its corresponding factors are 38, 1, and 11 pixels for subset radius, spacing, and strain radius respectively. To reduce computational costs, we can opt for solutions with lower desirability values, e.g. solution No. 38 with 68% desirability. Using this technique leads to an increase in computational speed with the factor of 2. In this way, strain measurement desirability has only 3% lowered in contrast to displacement optimization. The corresponding strain radius is 20 pixels.

#### 4. CONCLUSIONS

Novel structures employment requires a good knowledge of their behavior and accurate deformation measurement under the loading conditions. In the present paper, micro-structural deformation and field variable measurements are performed using digital image correlation during uniaxial compression tests. Finite element simulation of the actual lattice structure is also implemented for verification purposes. Also, CT-scan images and digital optical microscope images are used in modeling procedure by image processing. RSM and DOE techniques are also employed for optimization purposes. The most important applications of the present results are utilizing the labs with simple portable system to measure the deformation, strain, and stress fields, eliminating the measurement error of the contact experimental stress analysis methods, using DIC as a tool for health monitoring, tailoring the cellular solids by accurate determination of their mechanical properties, and using the present system for failure mode and localization determination in microstructures. Furthermore, we present the method of mesh and geometry refinement using the hybrid approach of CT-scan imaging and optical digital microscope image processing.

It is worth noting that we bridge between experiment-based measurement method (DIC) and numerical simulation (FEA). The main contribution is to present the hybrid methodology and strategy of verified measurement and field variables determination with minimized cost. Also, we present several correlation equations with experimental design and statistical methods for the main field variables, as well as DIC parameters optimization using response surface methodology. In addition, we optimize the computed tomography settings using the iterative approach. It yields to high-quality CT images with minimum artifacts to reach enhanced 3D model.

The main limitations and suggestions for future works are summarized below.

- We should use the controlled environment and dark boxes to minimize the illumination noise.
  - The present method could be applied only on specimens with high porosity because of their two-dimensional strain field.
  - Due to a large number of incremental images during axial loading, the image processing and DIC implementation are time-consuming.
  - We need the accurate micro-structural model in FE simulations for verification purposes.
  - Using two or more cameras for 3D strain tensor determination could be done in future.
  - Infra-red thermography is also could be added to the present system for failure mode and location determination.
- The most important results are summarized below:
- During the compression test, comprehensive DIC system implementation and analysis are done and major effective factors, e.g. illumination, rate of the capturing are identified.
  - 3D dynamic FE simulation is performed as a verification tool with detailed mesh sensitivity analysis for the continuous field calculation.
  - CT-scan images are obtained and processed and detailed 3D cellular models with accurate density values are modelled as FEM input.
  - Using CT-scan imaging with optimized settings instead of the expensive micro-CT for 3D modelling with acceptable accuracy is considered a novelty.
  - Digital microscope imaging is employed for foam model fine-tuning especially in cell edges and faces to reach the highest accuracy.
  - The relative error of DIC measurement and FEA results for vertical and horizontal displacements are 15 and 19%. The corresponding values for normal vertical and horizontal strain are 55 and 34%. This error for the shear strain is 65%.
  - Higher error for strain tensor is related to the numerical problems using derivation operator.
  - Normal vertical and horizontal strain component values are -1.08 and 1.6% and the shear strain is about 2.6 degrees in FEA.
  - Horizontal displacement is modelled using a quadratic correlation with ANOVA approach. To obtain higher accuracy results, the corresponding transformation power is 1.5.
  - vertical displacement is modelled using a quadratic correlation. The corresponding transformation power is -2.5.
  - To reduce the number of experiments, the central composite design approach of RSM is implemented and quadratic regression of displacement and strain field is obtained.

- Response surface methodology is employed to optimize DIC parameters such as subset reduce, subset spacing, and strain deduce.
- The most important factor in normal strain is the subset radius squared. Also, the most effective terms in shear strain prediction are strain radius and subset spacing squared.
- Displacement measurement optimization leads to 71% desirability with subset radius and spacing of 30 and 1 pixels respectively.
- Strain optimization with the highest desirability leads to subset radius, spacing, and strain radius of 38, 1, and 11.
- Considering computational cost and desirability of 68% together lead to similar factors with displacement measurement.

## 5. REFERENCES

1. Skozrit, I., Frančeski, J., Tonković, Z., Surjak, M., Krstulović-Opara, L., Vesenjajk, M., Kodvanj, J., Gunjević, B. and Lončarić, D., "Validation of numerical model by means of digital image correlation and thermography", *Procedia Engineering*, Vol. 101, (2015), 450-458. DOI: 10.1016/j.proeng.2015.02.054
2. Begonia, M.T., Dalls, M., Vizcarra, B., Liu, Y., Johnson, M.L. and Thiagarajan, G., "Non-contact strain measurement in the mouse forearm loading model using digital image correlation (dic)", *Bone*, Vol. 81, (2015), 593-601. DOI: 10.1016/j.bone.2015.09.007
3. Bernachy-Barbe, F., Gélébart, L., Bornert, M., Crépin, J. and Sauder, C., "Characterization of sic/sic composites damage mechanisms using digital image correlation at the tow scale", *Composites Part A: Applied Science and Manufacturing*, Vol. 68, (2015), 101-109. DOI: 10.1016/j.compositesa.2014.09.021
4. Mehdikhani, M., Aravand, M., Sabuncuoglu, B., Callens, M.G., Lomov, S.V. and Gorbatikh, L., "Full-field strain measurements at the micro-scale in fiber-reinforced composites using digital image correlation", *Composite Structures*, Vol. 140, (2016), 192-201. DOI: 10.1016/j.compstruct.2015.12.020
5. Whitlow, T., Jones, E. and Przybyla, C., "In-situ damage monitoring of a sic/sic ceramic matrix composite using acoustic emission and digital image correlation", *Composite Structures*, Vol. 158, (2016), 245-251. DOI: 10.1016/j.compstruct.2016.09.040
6. Gerbig, D., Bower, A., Savic, V. and Hector Jr, L.G., "Coupling digital image correlation and finite element analysis to determine constitutive parameters in necking tensile specimens", *International Journal of Solids and Structures*, Vol. 97, (2016), 496-509. DOI: 10.1016/j.ijsolstr.2016.06.038
7. Engqvist, J., Wallin, M., Ristinmaa, M. and Hall, S.A., "Modelling and experiments of glassy polymers using biaxial loading and digital image correlation", *International Journal of Solids and Structures*, Vol. 102, (2016), 100-111. DOI: 10.1016/j.ijsolstr.2016.10.013
8. Krstulović-Opara, L., Surjak, M., Vesenjajk, M., Tonković, Z., Kodvanj, J. and Domazet, Ž., "Comparison of infrared and 3d digital image correlation techniques applied for mechanical testing of materials", *Infrared physics & technology*, Vol. 73, (2015), 166-174. DOI: 10.1016/j.infrared.2015.09.014
9. Jiang, Y., Akkus, A., Roperto, R., Akkus, O., Li, B., Lang, L. and Teich, S., "Measurement of j-integral in cad/cam dental ceramics and composite resin by digital image correlation", *Journal of the Mechanical Behavior of Biomedical Materials*, Vol. 62, (2016), 240-246. DOI: 10.1016/j.jmbbm.2016.05.012
10. Nguyen, M.-T., Allain, J.-M., Gharbi, H., Desceliers, C. and Soize, C., "Experimental multiscale measurements for the mechanical identification of a cortical bone by digital image correlation", *Journal of the Mechanical Behavior of Biomedical Materials*, Vol. 63, (2016), 125-133. DOI: 10.1016/j.jmbbm.2016.06.011
11. Aparna, M.L., Chaitanya, G., Srinivas, K. and Rao, J.A., "Fatigue testing of continuous gfrp composites using digital image correlation (DIC) technique a review", *Materials Today: Proceedings*, Vol. 2, No. 4-5, (2015), 3125-3131. DOI: 10.1016/j.matpr.2015.07.275
12. Feng, X., Tufail, R.F. and Zahid, M., "Experimental investigation and statistical modeling of frp confined ruc using response surface methodology", *Civil Engineering Journal*, Vol. 5, No. 2, (2019), 268-283. DOI: 10.28991/cej-2019-03091243
13. Obianyo, J.I. and Agunwamba, J., "Efficiencies of horizontal and vertical baffle mixers", *Emerging Science Journal*, Vol. 3, No. 3, (2019), 130-145. DOI: 10.28991/esj-2019-01176
14. Sharif, S.H., Archin, S. and Asadpour, G., "Optimization of process parameters by response surface methodology for methylene blue removal using cellulose dusts", *Civil Engineering Journal*, Vol. 4, No. 3, (2018), 620-634. DOI: 10.28991/cej-0309121
15. Yang, K., Zou, J. and Shen, J., "Vibration and noise reduction optimization design of mine chute with foam aluminum laminated structure", *International Journal of Engineering, Transactions B: Applications*, Vol. 33, No. 8, (2020), 1668-1676. DOI: 10.5829/ije.2020.33.08b.26
16. Hosseini Ravandi, S., "Assessing of fabric appearance changes using image processing techniques", *International Journal of Engineering*, Vol. 12, No. 2, (1999), 99-106.
17. Fattahzadeh, M. and Saghaei, A., "A statistical method for sequential images-based process monitoring", *International Journal of Engineering*, Vol. 33, No. 7, (2020), 1285-1292. DOI: 10.5829/ije.2020.33.07a.15
18. Poissant, J. and Barthelat, F., "A novel "subset splitting" procedure for digital image correlation on discontinuous displacement fields", *Experimental Mechanics*, Vol. 50, No. 3, (2010), 353-364.
19. Li, X., Fang, G., Zhao, J., Zhang, Z. and Wu, X., "Local hermite (lh) method: An accurate and robust smooth technique for high-gradient strain reconstruction in digital image correlation", *Optics and Lasers in Engineering*, Vol. 112, No., (2019), 26-38. DOI: 10.1016/j.optlaseng.2018.08.022
20. Gonzalez, R.C., Woods, R.E. and Eddins, S.L., "Digital image processing using matlab, Pearson Education India, (2004).
21. Pan, B., Dafang, W. and Yong, X., "Incremental calculation for large deformation measurement using reliability-guided digital image correlation", *Optics and Lasers in Engineering*, Vol. 50, No. 4, (2012), 586-592. DOI: 10.1016/j.optlaseng.2011.05.005
22. Peretzki, E., Stockmann, M., Lehmann, T. and Ihlemann, J., "A new surface preparation method for microscopic digital image correlation applications", *Materials Today: Proceedings*, Vol. 12, (2019), 377-382. DOI: 10.1016/j.matpr.2019.03.138
23. Romans, L., "Computed tomography for technologists: A comprehensive text, Lippincott Williams & Wilkins, (2018).
24. Hsieh, J., "Computed tomography: Principles, design, artifacts, and recent advances, SPIE press, Vol. 114, (2003).
25. Kak, A.C. and Slaney, M., *Principles of computerized tomographic imaging. New york: The institute of electrical and electronics engineers*. 1988, Inc.
26. Wendt, R., *The mathematics of medical imaging: A beginner's guide*. 2010, Soc Nuclear Med.

27. Akar, A., Baltaş, H., Çevik, U., Korkmaz, F. and Okumuşoğlu, N., "Measurement of attenuation coefficients for bone, muscle, fat and water at 140, 364 and 662 keV  $\gamma$ -ray energies", *Journal of Quantitative Spectroscopy and Radiative Transfer*, Vol. 102, No. 2, (2006), 203-211. DOI: 10.1016/j.jqsrt.2006.02.007
28. Talebi, S., Sadighi, M. and Aghdam, M., "The effect of impact energy parameters on the closed-cell aluminum foam crushing behavior using x-ray tomography method", *AUT Journal of Mechanical Engineering*, Vol. 2, No. 1, (2018), 107-116. DOI: 10.22060/mej.2017.13385.5613
29. Talebi, S., Sadighi, M., Aghdam, M. and Mirbagheri, S., "Micro-macro analysis of closed-cell aluminum foam with crushing behavior subjected to dynamic loadings", *Materials Today Communications*, Vol. 13, (2017), 170-177. DOI: 10.1016/j.mtcomm.2017.10.004
30. Systemes, D., *Abaqus 6.9 documentation, dassault systemes simulia corp, providence, ri, USA*. 2009.
31. Jamshidi, Y.T., Anaraki, A.P., Sadighi, M., Kadkhodapour, J., Mirbagheri, S.M.H. and Akhavan, B., "Micro-structure analysis of quasi-static crushing and low-velocity impact behavior of graded composite metallic foam filled tube", *Metals and Materials International*, (2019), 1-14. DOI: 10.1007/s12540-019-00502-0

---

### Persian Abstract

---

#### چکیده

مواد متخلخل به ویژه فوم‌های فلزی با توجه به ویژگی‌هایی مانند نسبت استحکام به وزن و ارزش تصادف بالا، دارای جایگاه ویژه‌ای در میان مواد نوین هستند. از طرف دیگر سفارشی سازی این مواد مستلزم مشخصه‌یابی دقیق می‌باشد. در پژوهش حاضر، متدولوژی ترکیبی خاصی جهت شناسایی رفتار فوم‌های آلومینیومی ارائه شده است. از جمله دستاوردهای پژوهشی می‌توان به ادغام دو روش همبستگی تصاویر و اجزای محدود در اندازه‌گیری پیوسته میدان جابجایی و کرنش اشاره نمود. یکی از چالش‌های اساسی در شبیه‌سازی جامدات سلولی، مدلسازی ریزساختار آن و سپس تولید مش می‌باشد. برای حل این مشکل نیز از روش استفاده همزمان از تصاویر توموگرافی و میکروسکوپ نوری در فرآیند بازسازی هندسی استفاده شده است. پس از تولید نمونه‌های فوم فلزی و چیدمان سیستم تصویربرداری، نمونه‌ها تحت فشار محوری قرار گرفته و تصویربرداری با کیفیت انجام می‌شود. نهایتاً با استفاده از تکنیک همبستگی، میدان جابجایی و کرنش محاسبه می‌شود. از طرف دیگر به منظور صحت‌گذاری نتایج اندازه‌گیری و با هدف بهینه‌یابی تنظیمات روش همبستگی، به ترتیب از شبیه‌سازی عددی اجزای محدود با نرم‌افزار آباکوس همراه با مطالعه استقلال مش‌بندی و متدولوژی سطح پاسخ استفاده شده است. در نهایت معادلات همبستگی براساس مدل‌های رگرسیون مراتب بالا استخراج شده است. استفاده از مدل ریزساختاری و نیز پارامترهای بهینه روش همبستگی به تطابق مناسب میان نتایج شبیه‌سازی و تجربی منجر شده است. استفاده از تصویربرداری توموگرافی به همراه اصلاح جزئیات به کمک تصاویر میکروسکوپ نوری به جای میکرو سی تی، در عین حصول دقت مناسب، هزینه‌های تصویربرداری را به نحو چشمگیری کاهش می‌دهد.

---